Effects of process parameters on bead shape, microstructure, and mechanical properties in wire + arc additive manufacturing of $Al_{0.1}CoCrFeNi$ high-entropy alloy

Md.R.U. Ahsan [a], Gi-Jeong Seo [b], Xuesong Fan [c], Peter K. Liaw [c], Seyedamirhossein Motaman [d], Christian Haase [d], Duck Bong Kim [b,*]

[a] *Department of Mechanical Engineering, Tennessee Technological University, Cookeville, TN 38505, United States*
[b] *Department of Manufacturing and Engineering Technology, Tennessee Technological University, Cookeville, TN 38505, United States*
[c] *Department of Materials Science and Engineering, University of Tennessee, Knoxville, TN 37996, United States*
[d] *Materials Engineering of Metals, Steel Institute, RWTH Aachen University, 52072 Aachen, Germany*

A R T I C L E   I N F O

A B S T R A C T

The goal of this study is to investigate the wire + arc additive manufacturing (WAAM) of a high-entropy alloy (HEA) and to identify the near-optimal process parameters. To achieve the goal, a two-stage investigation is attempted using pre-alloyed and extruded $Al_{0.1}CoCrFeNi$ wire. In the first stage, single-layer beads are deposited with a range of process parameters (current, wire feed speed, and travel speed). Through process-signal monitoring, bead cross-section measurements, and statistical analysis, the threshold of energy density ($\geq$80 J/mm^3) for the uniform and continuous bead has been identified. In the second stage, thin-walled, multi-layer structures are deposited using two heat input conditions (low and high) with the same energy density. Large columnar grains with cellular dendritic substructures and a homogeneous composition are observed in both. Almost identical yield strength (260 MPa) and ultimate tensile strength (420 MPa) are measured with exceptional ductility (45–55%) for both deposits, which can be superior to casting and other AM processes. The high heat input is identified as the near-optimal processing condition, due to the improved surface quality, the higher ductility, and the higher deposition rate.

1. Introduction

Most commercial alloys are based on one principal element (e.g., Fe, Cu, Ni, and Al) used as the matrix with the minor addition of other elements to enhance properties and/or processability [1]. However, alloy development based on a single principal element has approached the limit for performance improvement and often involves a trade-off between desired properties such as strength and ductility [2]. Recently, a new alloy design strategy known as high-entropy alloys (HEAs) has emerged, which allows the mixing of five or more principal elements in equiatomic or near-equiatomic concentration [3,4]. Many HEAs exhibit exceptional properties including a combination of strength and ductility [2], high yield strength at elevated temperatures [5], and outstanding fracture toughness [3]. Due to the unique combination of remarkable mechanical properties, HEAs are gaining attention as a scope to develop materials with tailored properties for specific applications [1,3,6,7],

especially nuclear [8], power generation [5], and aerospace [9] industries.

Most of the research on HEAs has been focused on alloy development, material characterization, and post-processing [5,10–13]. Typically, these alloys are manufactured using conventional vacuum arc melting or induction melting followed by casting [14], and often require remelting, and post-processing steps to ensure homogeneity and desired properties [14]. Powder-metallurgy and plastic deformation-based techniques are also utilized. However, the aforementioned manufacturing techniques have several limitations in terms of cost, material efficiency, and freeform fabrication [15,16]. To provide cost-efficiency along with the flexibility of materials and structure geometries, additive manufacturing (AM) technologies have attracted considerable attention as an alternative path for fabricating HEAs [17].

Several AM methods have been successfully implemented to fabricate structures with HEAs [15,17–19]. The powder bed fusion (PBF)

processes, specifically the selected laser melting (SLM) technique, have been widely adopted [17,20–23]. Karlsson et al. [24] optimized the process parameters for SLM of AlCoCrFeNi HEA powder and compared the resultant microstructure and mechanical properties with induction melting. Unlike single-phase induction melted alloy, the SLM alloy consisted of a body-center-cubic (BCC) and ordered B2 structure [24]. Moreover, notable elemental segregation and a significant amount of cracks were reported [24]. The formation of cracks was attributed to thermal cycling, which leads to thermal stresses and segregation-driven phase transformations [24]. Nevertheless, no mechanical testing results were reported in that work. Zhou et al. performed SLM using the pre-alloy powder of $Al_{0.5}FeCoCrNi$, presenting a strong anisotropy in grain growth [25]. Another PBF process, the selective electron beam melting (SEBM) process, has also been widely applied for AM of HEAs [26]. SEBM of equimolar AlCoCrFeNi HEA resulted in BCC, B2, and FCC phases in the microstructure and exhibited an improved ductility over the induction melting alloy [26]. Among the direct energy deposition (DED) processes, laser metal deposition (LMD) with powder-feedstock has been reported with HEAs [27–29]. LMD of various HEAs also showed improved mechanical performance than the cast products [27,30].

Wire + arc additive manufacturing (WAAM), a wire-feed DED process, is reported to have high deposition efficiency and material utilization rates, and large-sized manufacturing parts [31,32]. WAAM can be categorized into the gas metal arc (GMA), gas tungsten arc (GTA), or plasma arc (PA) systems with respect to the different power sources [39]. Recently, Shen et al. [33,34] reported an innovative approach of combined cable wire arc additive manufacturing (CCW-AAM) using a cold metal transfer (CMT)-GMA system. The consumable CCW was composed of two Ni, two Al, one Fe, one Co, and one 304 stainless steel (~70% Fe, ~20% Cr, ~10% Ni) wires [34]. The authors reported a comparable compressive strength to cast HEA with improved ductility in thin-walled structures, exhibiting the feasibility and potential of WAAM of HEA [34]. However, the aforementioned work is based on a CMT process, which works on a consumable-specific synergic program [35]. The current and voltage values are determined by the program based on the wire feed speed [36]. It is unclear from the work whether a consumable specific synergic program was developed or not. In the CMT process, the actual current and voltage are often adaptively varied by the machine to maintain a constant deposition rate. Depositing HEA with a program for other material may result in a thermal field leading to an undesirable microstructure, and thus, undesirable properties [34].

Despite higher deposition rates in GMA-WAAM [40], GTA- and PA-WAAM processes [39,41] are more suitable for working with experimental materials like HEAs and determining the optimal process parameters, due to the required independent control of the power setting and wire-feed speed [42]. The GTA-WAAM process is utilized for the present study [40] to investigate WAAM with pre-alloyed HEA wire feedstock [25]. The $Al_xCoCrFeNi$ (x in molar ratio) [37] family of HEA exhibits outstanding tensile strength [38], ductility [5], and corrosion resistance [39], and has the potential for future applications in high temperature and corrosive environments. As the $Al_xCoCrFeNi$ HEA family is widely investigated, the present study is focused on using an $Al_{0.1}CoCrFeNi$ alloy to compare GTA-WAAM with different manufacturing processes.

Due to the unavailability of any prior data on the effect of process parameters on the bead geometry, several conditions for deposition of single-layer beads are developed using a design of experiments (DOE) approach with a range of welding currents, travel speeds (TS), and wire feed speeds (WFS). Based on the statistical analysis of the bead cross-sections, and in-situ process monitoring, the minimum required energy density for the continuous and uniform bead is identified in Section 3.1. Later, the microstructure and mechanical properties of two thin-walls deposited with low and high heat inputs are analyzed in Section 3.2. Lastly, the results from two deposits are compared and discussed in contrast with casting and other AM processes; and the near-optimal

process parameters for GTA-WAAM of $Al_{0.1}CoCrFeNi$ HEA are identified in Section 4. The understanding of the relationship between processes and properties developed in this work can be further utilized for a future in-depth study on the same alloy or to identify near-optimal process parameters for different HEAs.

2. Methods

2.1. GTA-WAAM system

All the experiments were performed using a GTA-WAAM system developed in-house, as shown in Fig. 1. The setup consists of a 6-axis Fanuc ArcMate 100ib robot arm with a Fanuc R-J3iB controller, a Miller Dynasty 400 GTA welding power source, and a generic wire feeder. The travel speed (TS), welding current (Current), and the wire feed speed (WFS) are individually controlled through the robot, power source, and wire feeder, respectively. The welding voltage is analogous to the gap between the electrode tip and the workpiece or the substrate. All the experiments for this work were conducted with a constant gap of 5 mm and an argon shielding.

2.2. Material

To fabricate the $Al_{0.1}CoCrFeNi$ substrate and wire, first, the constituents were melted in a vacuum induction furnace at the composition presented in Table 1. To fabricate a substrate, the molten metal was cast into a 500 mm × 100 mm × 25 mm block and then exposed to hot isostatic pressing (HIP). For the wire feedstock, the molten metal was cast into cylindrical ingots. Later, these ingots were HIPed and machined into 200 mm long billets with a 50 mm diameter. The billets were extruded to a 22 mm diameter. From the extruded billets, the HEA consumable with a 1.2 mm diameter was drawn at 871 °C. The detailed steps involved in the whole fabrication process are presented in Fig. 2.

2.3. Deposition conditions and in-situ process monitoring

To study the effects of process parameters on deposition quality as well as to identify the near-optimal process parameters, a two-stage experiment approach was devised. For the first stage, the three factors of Current, TS, and WFS were considered, and single layers of materials were deposited on the substrate with a range of conditions. Based on statistical analyses and process monitoring of these single-layer deposits, the process window was identified. Using this process window, multiple layers were deposited to fabricate thin-wall structures in the second
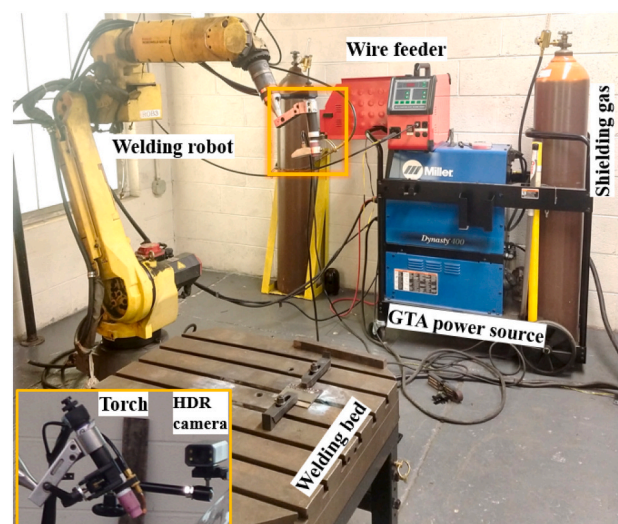

Fig. 1. The GTA-WAAM system with the different components identified.

Table 1
Composition of the high-entropy alloy substrate and wire.

Alloying elements	Al	Co	Cr	Fe	Ni
Composition (wt%)	1.18	25.83	22.79	24.48	25.72
Composition (at.%)	2.44	24.39	24.39	24.39	24.39

stage.

The welding current and voltage were monitored using a Miller Insight ArcAgent™. The current and voltage sensors were attached to the welding system, and the data were recorded in real-time on a computer at a sampling rate of 3000 Hz. From the monitored data, the time of any change of current or voltage can be identified. Thus, process instability, or bead discontinuity/irregularity, can be found and explained based on the measured process signatures.

2.4. Analyses of bead shapes, microstructures, and mechanical properties

The single-layer deposits, or beads, were first investigated from the images taken from the top for uniformity. Later, the beads were cross-sectioned in three different locations. These cross-sections were ground and polished, following the general metallography procedure [40]. For etching, a glyceregia solution (3 parts of HCl, 2 parts of glycerol, and 1 part of HNO_3) was used. The etched samples were observed using a Nikon SMZ 1500 optical microscope (OM). The bead height, width, and toe angle were measured from the OM results as seen in Fig. 3, using the Image-J software [41].

Using the same procedures above, metallographic specimens were prepared from the thin-walled structures. An FEI Quanta 200 scanning electron microscope (SEM) with an energy-dispersive X-ray spectroscopy (EDS) attachment was used for microstructural and chemical composition analysis. The electron back-scattered diffraction (EBSD) analysis was performed using Zeiss EVO MA15 equipment with a Bruker eFlash EBSD detector. Later, the ATEX software [42] was used for post-processing and analyzing the EBSD data. In addition, microhardness tests were performed using a Buehler Micromat II tester (Vickers diamond indenter) with a 500 g load.

From the thin-walled structures, tensile test specimens were prepared using wire electrical discharge machining (wire-EDM) with dimensions specified in the American Society for Testing and Materials (ASTM) E8 standard [43]. The mechanical performance was investigated through the computer-controlled, uniaxial tensile testing system (MTS 810 servo-hydraulic machine). From each thin-walled structure, three samples were tested with a strain rate of 10^{-3} s^{-1}. To determine the failure characteristics and evaluate the presence of anomalies, the fractured locations, surfaces, as well as modes, were investigated using the OM and SEM.

3. Results

3.1. First stage: single layers

For the single-layer depositions in the first stage, the distance between the electrode tip and substrate, shielding gas flow rate, and travel distance were maintained constant at 5 mm, 20 l/min, and 100 mm, respectively. The factors in consideration (Current, TS, and WFS) were
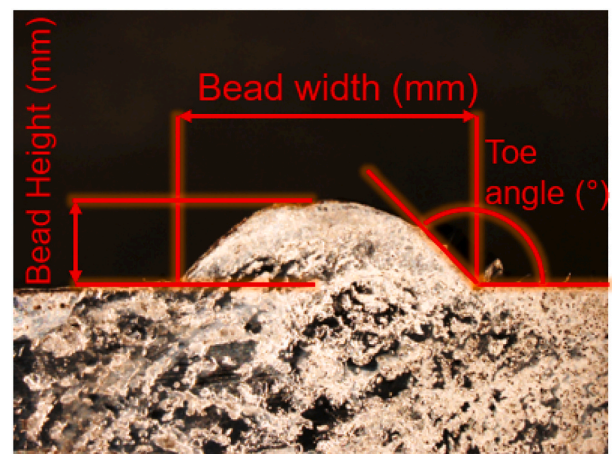

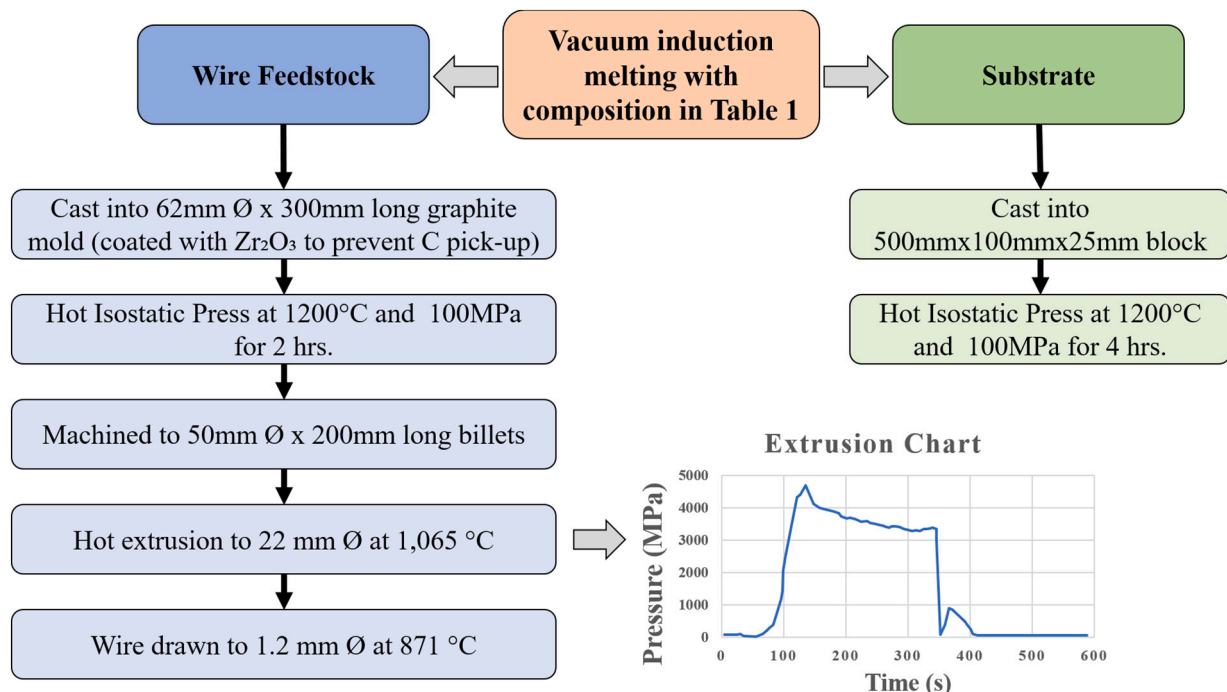**Fig. 3.** Responses considered for the first stage of experimentation.

Fig. 2. Flow diagram showing the steps for fabricating the substrate and the wire feedstock.

assigned to three levels as shown in Table 2. A full factorial design, considering all possible conditions, will result in 27 experimental conditions. Owing to the limited availability of materials, the Taguchi method was selected to efficiently reduce the number of experiments [44]. The L₉ (3³) orthogonal array of the experimental conditions can be seen in Table 3. For all conditions, heat input and energy density were calculated using Eqs. (1) and (2), respectively. For each condition, the current was obtained from the set value at the GTA power source. As the gap between the tungsten electrode and the substrate was set at 5 mm, the voltage was supposed to be constant at 15.5 V. However, fluctuation in voltage signal was observed in the monitoring. Hence, the voltage value was obtained by averaging the measured voltage data from the monitoring system.

$$\text{Heat input (J/mm)} = \frac{\text{Current} \times \text{Voltage}}{\text{TS}/60} \qquad (1)$$

[45]

$$\text{Energy density (J/mm}^3) = \frac{\text{Current} \times \text{Voltage}}{\frac{\pi \times (\text{radius of the wire})^2 \times \text{WFS}}{60}} \qquad (2)$$

[45]

3.1.1. Correlating the bead continuity with in-situ monitoring

The corresponding single-layer beads for C1–C9 can be seen in Fig. 4 (a). The visual observation shows that, among the single-layer deposits, C3 is discontinuous with periodic spherical deposits, called "balls." C2 has a continuous bead with an extremely narrow profile. Despite having continuous depositions, the bead profile is not uniform in C5 and C7. The rest of the conditions produce uniform weld beads.

As a constant current GTA welding process was used, the current signature remained stable during the deposition. In contrast, significant fluctuations in the voltage signature are observed depending on the material transfer mode and formation of discontinuity [46]. Similar observations have also been reported in prior studies involving the monitoring of welding processes [48,49,68]. Based on the voltage monitoring data and the material-transfer modes, the quality of the deposition for all these conditions can be explained and justified [46]. Hence, the corresponding voltage signatures of the marked sections in Fig. 4(a) are presented in Fig. 4(b).

In GTA-WAAM, the arc length (the distance between the electrode tip and the workpiece) governs the voltage [67]. The consumable wire is fed in between this space. Depending on the process parameters, two different material-transfer modes with different voltage waveforms can be achieved: (i) intermittent or droplet and (ii) uninterrupted or bridge [46]. In the intermittent transfer, the periodic rise and fall of the voltage are observed, while the voltage signatures remain comparatively flat in the bridge transfer [47]. Among the deposition conditions, C1, C2, C3, C5, and C6 show a periodic rise and fall of voltage, indicating an intermittent transfer. The intermittent transfer occurs at a low heat input and energy density. C2, C3, and C5 have the lowest values for these two parameters. Due to the extremely low heat input, C3 produces a discontinuous bead. Despite an intermittent transfer in C1, C2, C5, and C6, the adequate energy density and heat input allow the molten metal to form a continuous uniform bead in these conditions.

Among the other conditions, C7 has a continuous bead and relatively flat voltage signatures, suggesting the bridge transfer. However, the

Table 2
Experimental factors and levels.

Factor(s)	Factor level(s)		
	1	2	3
Current (A)	150	200	250
TS (mm/min)	200	400	600
WFS (mm/min)	1500	2000	2500

Table 3
Experimental L₉ (3³) orthogonal array with the heat input and energy density.

Condition	Current (A)	Average voltage (V)	TS (mm/min)	WFS (mm/min)	Heat input (J/mm)	Energy density (J/mm³)
C1	150	15.53	200	1500	697.50	82.23
C2	150	14.45	400	2000	325.13	57.49
C3	150	15.94	600	2500	239.10	50.74
C4	200	16.06	200	2000	963.60	85.20
C5	200	16.44	400	2500	493.20	69.77
C6	200	17.08	600	1500	341.60	120.82
C7	250	16.70	200	2500	1252.50	88.60
C8	250	17.78	400	1500	666.75	157.21
C9	250	18.26	600	2000	456.50	121.09

bead profile is not straight. As seen in Table 3, C7 has an extremely high heat input. As a result, the temperature of the molten metal will also be high. The surface tension and viscosity of molten metal, which are responsible factors governing the bead shape, decrease with increasing temperature [36,48]. The low surface tension and viscosity allow the molten metal to spread out and form non-uniformity in the bead.

The voltage signatures of C4, C8, and C9 suggest the bridge transfer. This trend is coupled with adequate energy density and heat input to form the uniform beads. It should be noted that the voltage signatures can also be used for detecting any minor discontinuities in the beads. There are minor discontinuities on the bead, as marked in Fig. 4(a). Matching the time with the voltage signatures also shows a fluctuation. The same observations are seen in C4, C6, and C7. There is one particular fluctuation in the signature of C9. The sudden rise of the voltage may indicate the reignition of the arc, but no discontinuity in the bead is visible.

3.1.2. Effect of process parameters on the bead geometry

To study the effect of individual process parameters on the bead geometry and identify a universal process window in terms of unified process parameters (i.e., heat input and energy density) for the HEA in use, analysis of variance (ANOVA) is performed using the bead cross-section measurement data (bead width, height, and toe angle) presented in Table 4. The Minitab® software (version 17) is used for ANOVA, and the results are graphically presented in Fig. 5.

The bead width tends to increase with the current and decreases with the TS and WFS. The heat input and energy density both increase with current, consequently increasing the amount and the temperature of the molten metal. Due to the low viscosity and surface tension at high temperatures [36,48], the molten metal can spread out more with high heat input and causes the continuous increase of the bead width. In contrast, increasing the TS reduces the amount of heat input [49]. Also, with faster TS, the same amount of molten metal is deposited over a larger area. The combination of the mentioned trends results in a smaller bead width with increasing TS. According to Eq. (2), an increase in the WFS reduces the energy density if the other parameters are unchanged. As the same amount of energy is being used for melting a greater amount of material, the temperature of the molten metal decreases. The lower temperature of the molten metal leads to a faster solidification, which prevents the molten metal from spreading out. The bead width decreases with the increase in WFS.

The bead height initially increases with current (150 to 200 A) and then decreases to the minimum at the high current (250 A). By increasing the current from low to medium values, both the heat input and the amount of molten metal increase, and thus, the bead height also increases. However, the extremely low surface tension and viscosity at high current [48,49] result in a flat bead profile, causing the bead height to decrease. Due to the trend for the total amount of deposited material to decrease with increasing TS, the bead height gradually decreases with TS. The initial increase in the amount of material deposited with WFS coupled with faster solidification lead to an increase in the bead height.
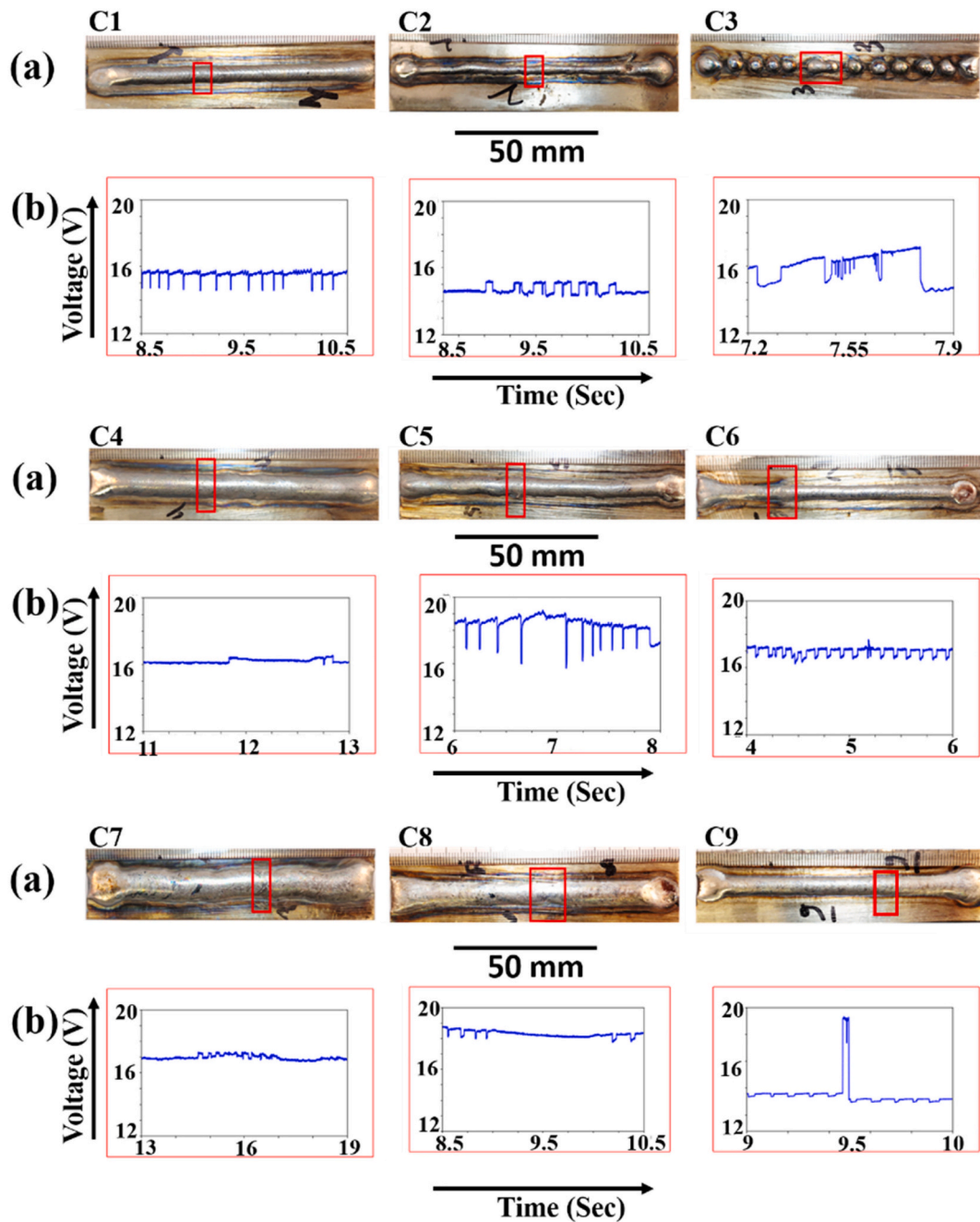
Fig. 4. Top view of single-layer deposits with voltage-monitoring data of the marked section.

Table 4
Measured responses for the first level of experiments.

Condition	Average bead width (mm)	Average height (mm)	Average toe angle (°)
C1	6.02	1.67	132.99
C2	3.81	1.71	112.06
C3	0.00	0.00	180.00
C4	7.77	1.46	138.57
C5	5.87	1.41	139.98
C6	6.62	1.01	153.99
C7	11.12	1.55	148.78
C8	5.80	0.47	161.63
C9	6.28	0.84	153.14

However, a further increase in WFS may result in an energy density too low to sustain the same rate of melting of the wire. The lower amount of the molten metal is assumed to be responsible for the decrease in the bead height at the high WFS.

The toe-angle effect is dependent on both the bead height and bead width. By increasing the bead height, the tow angle decreases, whereas the toe-angle increases with the bead width. The toe-angle in the present work follows the same increasing trend as the bead width for the current. Initially, by increasing the TS, the bead width and height decrease almost identically. As a result, the toe angle remains almost unchanged. However, at the high TS, the bead height drops more than the bead width, causing the toe angle to increase. As the effect of WFS is more significant on the bead height, the trend of the toe angle inversely follows the bead height, first decreasing to a minimum and then again increasing.
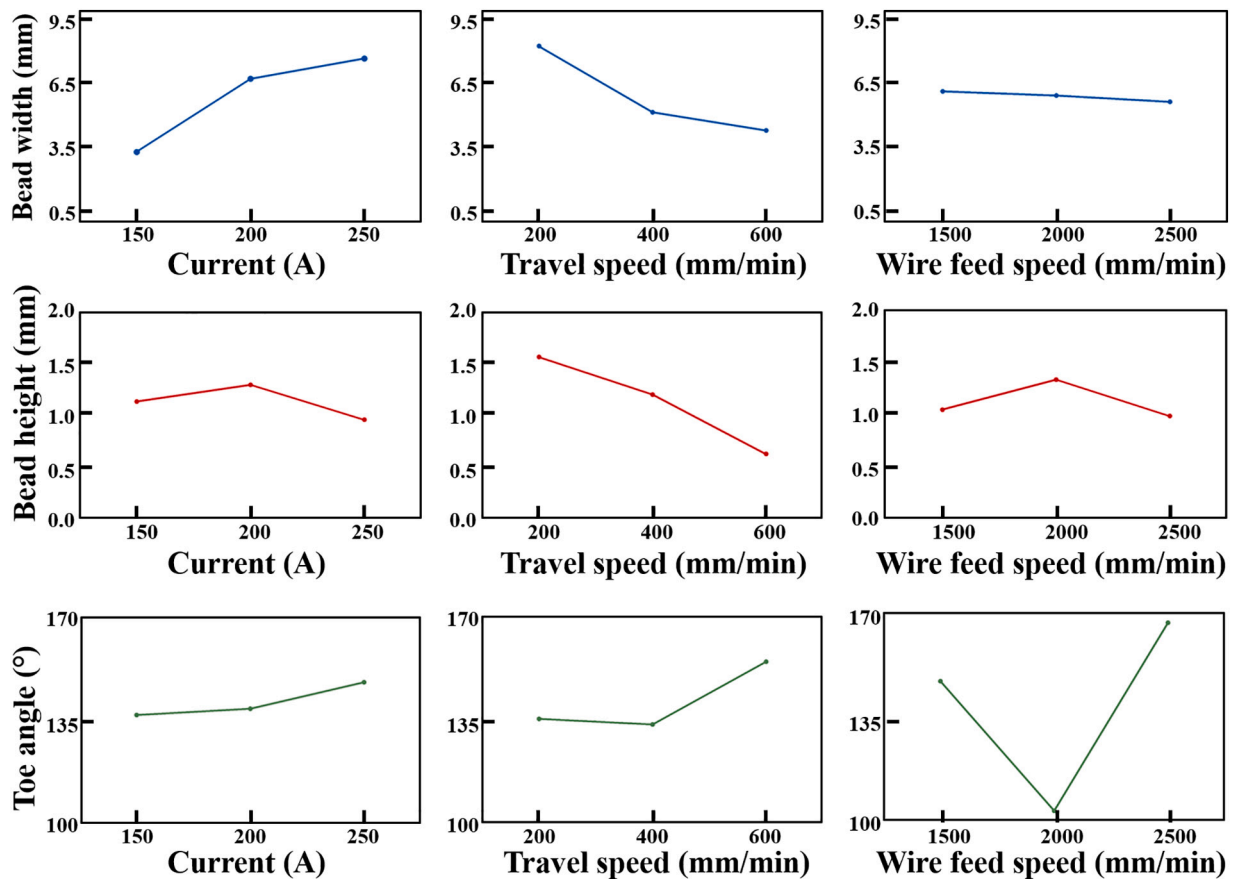
Fig. 5. ANOVA results showing a significant correlation among factors, factor levels, and responses.

To identify a universal process window for the HEA in use, the main effects and interactions of the heat input and energy density on bead height and width are graphically presented in Fig. 6. As seen in Fig. 6(a), the effect of heat input on the bead height is random. In contrast, the bead height shows a decreasing trend with increasing energy density, whereas the bead width roughly increases with increasing heat input and energy density (Fig. 6(b)). To attain further understanding in terms of any interaction between the factors, interaction plots are generated for both responses (Fig. 6(c) and (d)). Interaction plots show that the energy density is the main factor for the bead height and width. With increasing energy density, more energy is transferred to the same amount of wire, increasing the temperature of the molten metal. Due to the inversely proportional relationship of the surface tension and viscosity with temperature [49], the bead height decreases, and the bead width increases with the increasing energy density. However, the bead width starts to decrease beyond the energy density value of 88 J/ mm^3. The process parameters in Table 3 show that the conditions with the low bead width are C6 (A: 200, TS: 600 mm/min, and WFS: 1500 mm/min), C8 (A: 250, TS: 400 mm/min, and WFS: 1500 mm/min), and C9 (A: 250, TS: 600 mm/min, and WFS: 2000 mm/min). All these conditions have low to medium WFS with medium to high TS. As a result, less material is being deposited over a larger area, and the bead width decreases.

From these analyses and the results from Section 3.1.1, it is decided that an adequate energy density is the main factor for depositing uniform and continuous beads. In contrast, the droplet-transfer mode and heat input are minor factors. An energy density higher than 80 J/ mm^3 is repeatedly observed to produce a quality weld bead except for C7. The extremely high heat input in this particular condition is deemed responsible for the non-uniformity. Accordingly, this threshold of energy density is maintained in the second stage of experimentations.

3.2. Second stage: thin-walled structures

The conditions forming continuous and uniform beads (C1, C4, C6, C8, and C9) have a range of parameters (Current: 150, 200, and 250A; TS: 200,400 and 600 mm/min.; WFS: 1500 and 2000 mm/min), as listed in Table 3. However, a closer look at the conditions shows that several combinations of these parameters are unsustainable. Despite forming a uniform bead at 150A in C1, the medium or high WFS can result in an inadequate energy density at this current. The high WFS (C3, C5, and C7) did not produce a quality weld bead. Depending on the energy density, all three TS produce quality beads. The low TS can produce a quality bead at the cost of a slow deposition rate, which is undesired. Hence, only the medium and high TS are considered for further study. Based on these considerations, the medium WFS (2000 mm/min) and current (200 A) in combination with the medium and high TS are considered. Using these parameters, two experimental conditions with the same energy density but different heat inputs: (i) low heat input (LHI) and (ii) high heat input (HHI) are selected, as shown in Table 5. Using two conditions, thin-walled structures are deposited, as seen in Fig. 7. In the following subsections, each of these deposits is analyzed in terms of (1) material efficiency and surface quality, (2) microstructure analysis, and (3) mechanical properties.

Previous studies suggest that a continuous deposition in WAAM results in temperature buildup [35,50,51]. As a result, heterogeneous properties within the same structure can form. This trend may also cause the molten metal to drip off in later layers, causing a serious deterioration in the build quality [35,50,51]. Hence, an intermittent deposition approach was adopted in the present work. After the deposition of each layer, the top surface was allowed to cool down to 200 °C before depositing the next layer. The temperature was monitored by placing a *k* type thermocouple on the surface of the deposited layer.
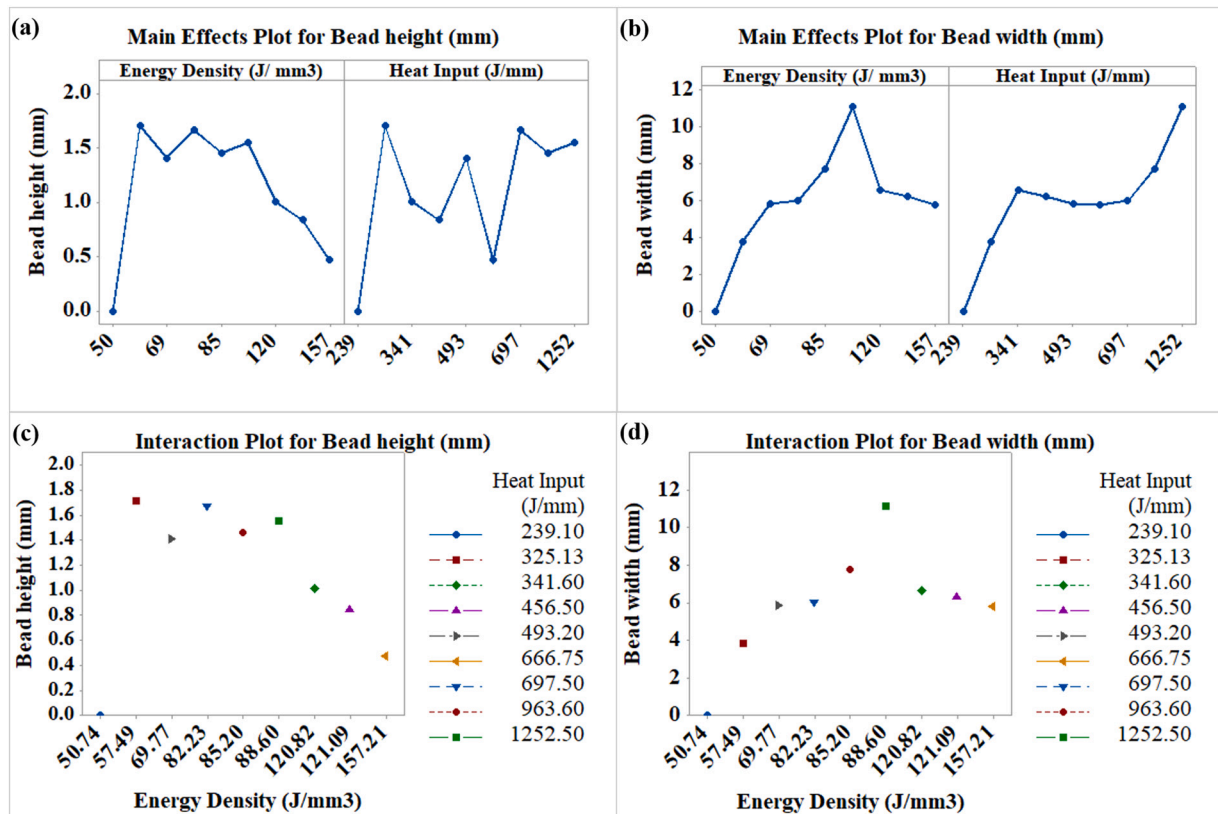
Fig. 6. Main effects plot (a) for bead height and (b) bead width showing correlation with energy density and heat input. Interaction plots for (c) bead height and (d) bead width.

Table 5
Process parameters for the multi-layer samples.

Condition	Heat input (J/mm)	Current (A)	Set voltage (v)	WFS (mm/min)	Energy density (J/mm³)	TS (mm/min)
i. (LHI)	310	200	15.5	2000	82.23	600
ii. (HHI)	930					200

3.2.1. Material efficiency and surface quality

For both deposits, the surface roughness and material efficiency were measured from the cross-sections in Fig. 8(a). From the cross-section, the outlines for both deposits were depicted using Image-J, as presented in Fig. 8(b). Within the outline, the largest possible rectangle with parallel arms was drawn. Later, the ratio of the area of the drawn rectangle and the total cross-section area was calculated, which can be interpreted as material efficiency.

For the measurement of surface roughness (R_a), the ISO 4287:1997 standard [52] was followed. A mean line was drawn on each side of the deposits. From the mean line, the deviation of the actual surface was measured at multiple locations at 1 mm apart. Later, the surface roughness was calculated, based on Eq. (3)

$$Ra = \frac{1}{lr}\int_0^{lr} |z(x)dx| \tag{3}$$

[52], where l_r stands for the sampling length.

The minimum required machining and the surface roughness are graphically compared in Fig. 8(c). The HHI deposit exhibits better material efficiency and surface quality than the LHI. A similar tendency of the surface quality to improve with HHI is also observed in the previous
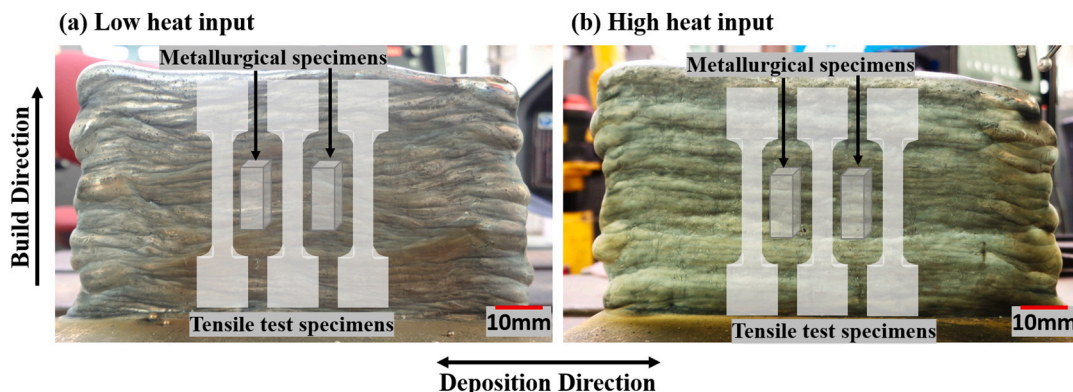

Fig. 7. Multi-layer thin-walled deposits with (a) low heat input and (b) high heat input.
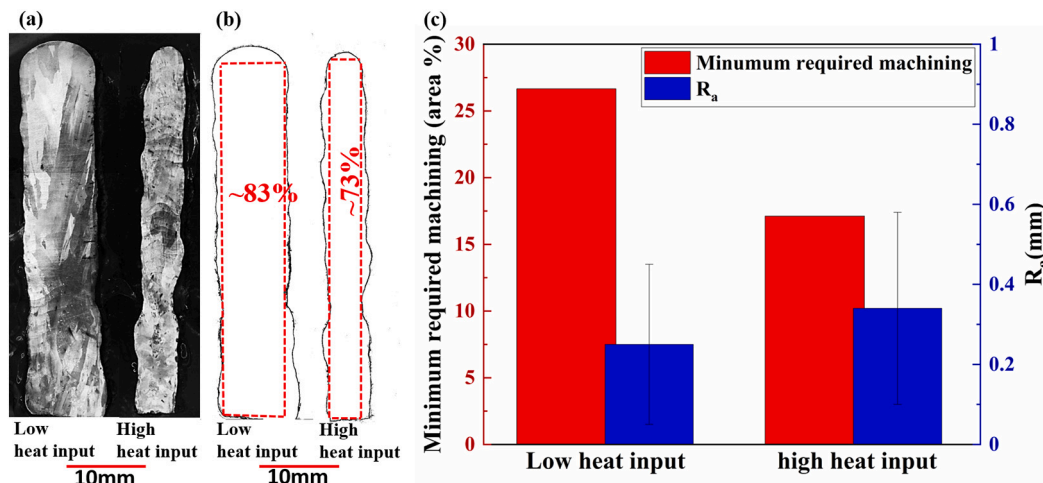
Fig. 8. (a) Cross-sections of the deposited walls with both heat input conditions, (b) the outline of the deposits with the largest possible rectangular area marked with dotted red lines, and (c) graphical representation of minimum required machining and R_a for both deposits. (For interpretation of the references to color in this figure legend, the reader is referred to the web version of this article.)

research with other materials [53,54].

During the GTA-WAAM process, the combined effect of the arc pressure and the momentum of the droplet pushes the molten metal to the back of the molten pool [53]. In the LHI condition, the molten pool is long and narrow that the solidification occurs fast. This trend prevents the flow of molten metal and creates an uneven surface [53]. Although the heat input can be increased by raising the current, the resulting stronger arc blow may contribute to further deterioration of the surface quality [53]. In contrast, increasing the heat input through reduced TS helps improve the surface quality by forming a wider melt pool and delaying the solidification [53]. At a higher heat input, the ratio between the width to the height also increases for each deposited layer, which further improves the surface quality by forming a smoother contour with the previous layer [54]. Since the heat input is manipulated by controlling the TS in this study, improved surface quality and material efficiency are obtained at HHI.

3.2.2. Microstructure

The EBSD analysis and backscattered electron (BSE) SEM results along with the elemental mapping are presented in Figs. 9 and 10, respectively. The EBSD grain maps in Figs. 9(a)-(i) and (ii) show that both heat input conditions exhibit very large columnar grains. However, the grain maps show some grain boundary-like features within the same grains. The inverse pole figure (IPF) X-maps in Figs. 9(b)-(i) and (ii) show that the regions marked as one single grain in the grain map consist of multiple columnar subgrains with almost identical orientations. For further clarification, the misorientation distribution in the marked sections of Fig. 9(b) is analyzed and presented in Fig. 9(c). The misorientation is measured with respect to the initial points (leftmost point) and shows a sharp increase in misorientation angle at the grain boundaries visible from the grain maps. Although smaller in magnitude, a change in the misorientation angle is also observed at the subgrain boundaries for both deposits. This confirms that the regions identified as a single grain in the grain maps in Fig. 9(a) consist of multiple subgrains. The average grain size in both deposits are also measured from the EBSD data and presented in Fig. 9(d), showing that the HHI deposit has significantly larger grains than the LHI one. To later relate the mechanical properties to the microstructure, the geometrically necessary dislocation (GND) density is analyzed for both deposits from the EBSD data as shown in Fig. 9(e). GNDs form due to the texture of material and stress and can result in macroscopic strengthening. The color difference between the GND density maps suggests that the LHI deposit has a higher dislocation density. Due to the difference in the heat input and, thus, the processing thermal fields, the HHI deposit reaches a higher

temperature for a longer time, leading to larger grains with lower dislocation density. It should also be noted that the GND density is higher at the grain boundaries compared to the subgrain boundaries for both deposits.

The SEM micrographs of the layer interface for both heat input conditions are presented in Fig. 10(a)-(i) and (ii). In both micrographs, dendritic substructures are observed. A similar microstructure is also observed in the welding of the same HEA [55]. In the study of the effect of Al addition on the microstructure, Wang et al. [56] also reported the formation of columnar grains with dendritic substructures in HEAs with similar compositions. The dendritic substructures in the LHI sample appear to be equiaxed, whereas the HHI sample has larger columnar dendritic substructures. It should be noted that the layer interface can be visually identified for both specimens through the discontinuity in the dendritic substructures. To ensure a compositional homogeneity, the EDS analysis with the line-scan was performed at the layer interface, as seen in Fig. 10(b)-(i) and (ii). Although fluctuation in the elemental distribution is observed, macroscopic elemental segregation is not observed and mean chemical composition remains constant. However, the LHI sample exhibits relatively higher fluctuations in the elemental distribution than the HHI one. The improved compositional homogeneity at HHI is attributed to the higher temperature of the deposition condition, which allows elemental diffusion, mostly back-diffusion from interdendritic regions resulting in partial homogenization [5].

3.2.3. Mechanical properties

3.2.3.1. Microhardness test results.
To estimate the hardness, a micro-Vickers test is performed in the build direction on both deposits, and the resulting hardness profiles are presented in Fig. 11. The hardness values range from 140 to 190 HV, which suggests a material with low strength and potentially high ductility. A similar hardness value was reported in the welding of the $Al_{0.1}CoCrFeNi$ HEA [55]. It should be noted that the HHI deposit (HV: 161 ± 9) has a slightly lower hardness than the LHI deposit (HV: 168 ± 8), which stems from the larger grain size and lower initial dislocation density as seen in Fig. 9. The smaller grain size and higher dislocation density increase the hardness of metals [57–59] and are identified as the reason behind the higher hardness values at LHI in this study.

3.2.3.2. Uniaxial tensile properties and fractography.
Three tensile specimens for each heat-input condition were tested with a strain rate of $10^{-3} s^{-1}$. As shown in Fig. 12(a), the yield strength (YS) and the ultimate
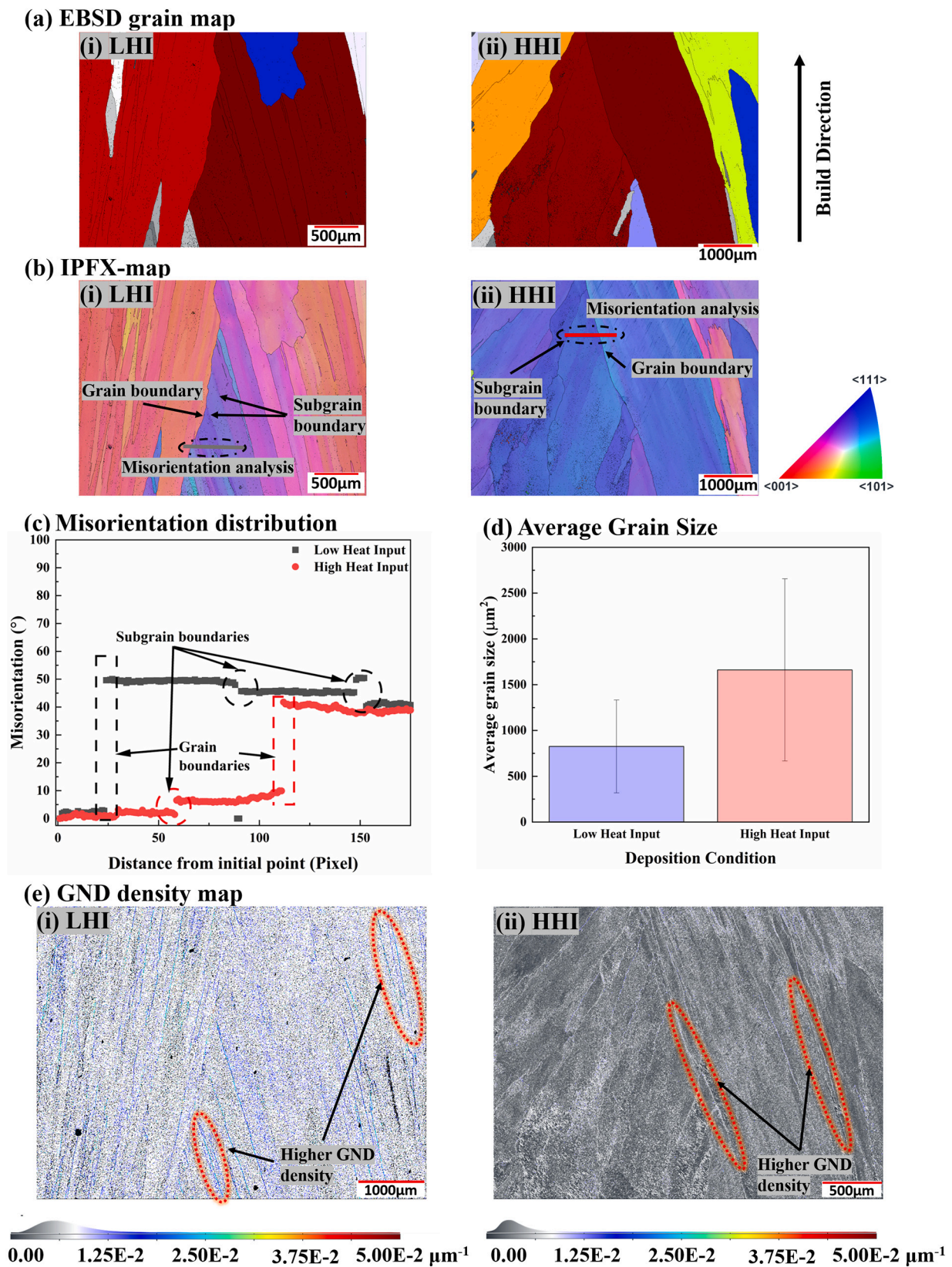
Fig. 9. (a) EBSD grain map; (b) IPFX-map with the line for misorientation distribution analysis showing (i) low heat input and (ii) high heat input deposits; (c) representative misorientation distribution; (d) average grain size; and (e) geometrically necessary dislocation (GND) density distribution with color-coded density scale.
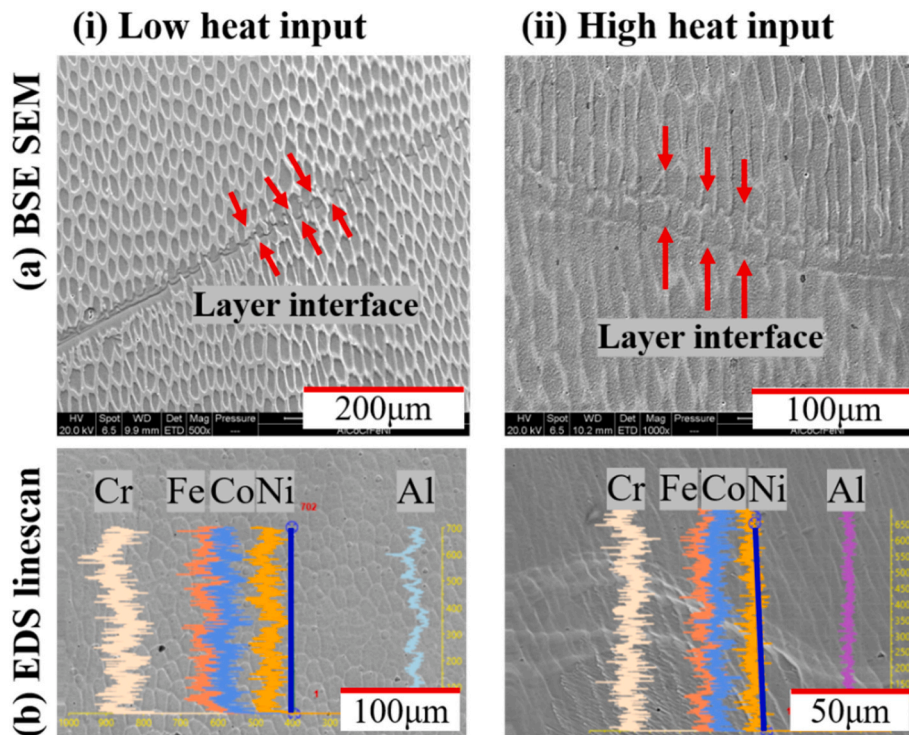
Fig. 10. Microstructure and compositional analysis results on the thin-walled multi-layer deposit with both heat input conditions.
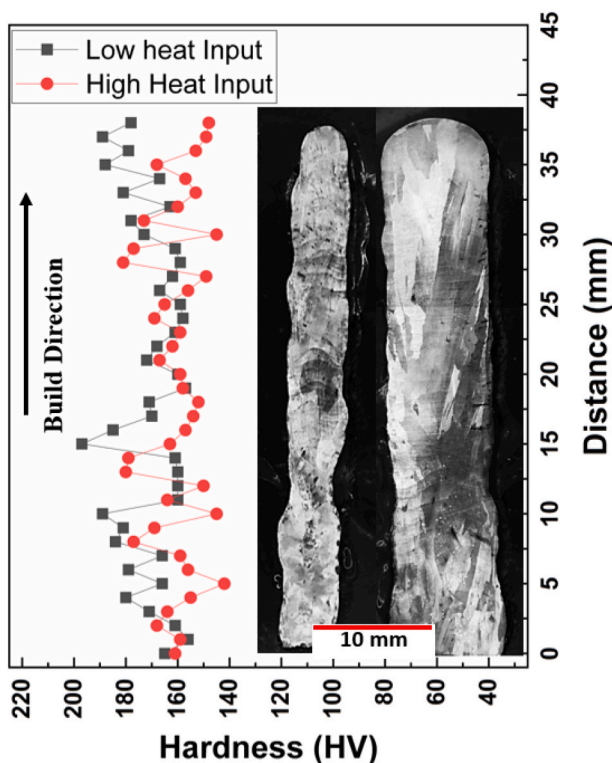

Fig. 11. Hardness profiles of HEA deposits with low and high heat-input conditions.

tensile strength (UTS) for both conditions showed similar values and were about 260 ($\pm$10) MPa and 420 ($\pm$6.50) MPa, respectively. Similar results have also been reported in a cast and HIPed $Al_{0.1}CoCrFeNi$ HEA [60,61]. The results also show that the WAAMed specimens have outstanding ductility with the tensile strain of ~50% as assumed from

the hardness test results in the previous section. It should be noted that GTA-WAAM deposits induce significantly higher ductility, compared to other AM processes [62,63].

To complement these results, the failure locations and the fracture surfaces are analyzed and presented in Fig. 12(b)–(d). The failure locations in Fig. 12(b) show angles close to 45°, similar to other ductile materials [64]. The low magnification image of the fracture surface of the LHI specimen (Fig. 12(c-i)) shows the significant deformation. The high magnification images from the center and edge in Fig. 12(c)-(ii) and (iii) demonstrate predominantly dimple-like features, suggesting a ductile failure through microvoid coalescence [64]. The fracture surface of the HHI specimen has a similar appearance (Fig. 12(d)). However, the size of the dimple-like features in the HHI specimen is slightly larger than that in the LHI specimen at the same magnification.

4. Discussion

4.1. Effects of process parameters on bead geometry

Although the effects of process parameters on bead geometry have not been reported for WAAM of HEA, similar studies are performed on WAAM of other power sources and materials [65,66]. In GTA-WAAM of Ti64 and Inconel718 [66], the bead width is reported to increase with current similar to the present work. However, the effect of current on bead height did not show a clear trend [66]. In both GMA-[66] and GTA-[65] WAAM, the bead height and width are reported to decrease with the increasing TS, which is also observed in Fig. 5. In the present work, the bead width decreases with increasing WFS, whereas the height initially increases and then decreases to a minimum at high WFS. As the prior work on GTA-WAAM [65] does not address the effect of WFS on bead shape, a direct comparison cannot be made. In GMA-WAAM, the bead height is reported to have a similar decreasing trend with WFS, while the bead width gradually increases [44]. This bead height trend does not match the data shown in Fig. 5. However, it should be noted that the GMA-WAAM work mentioned is limited to a WFS of 290 mm/min [44], which is much lower than the range (1500 to 2500 mm/min)
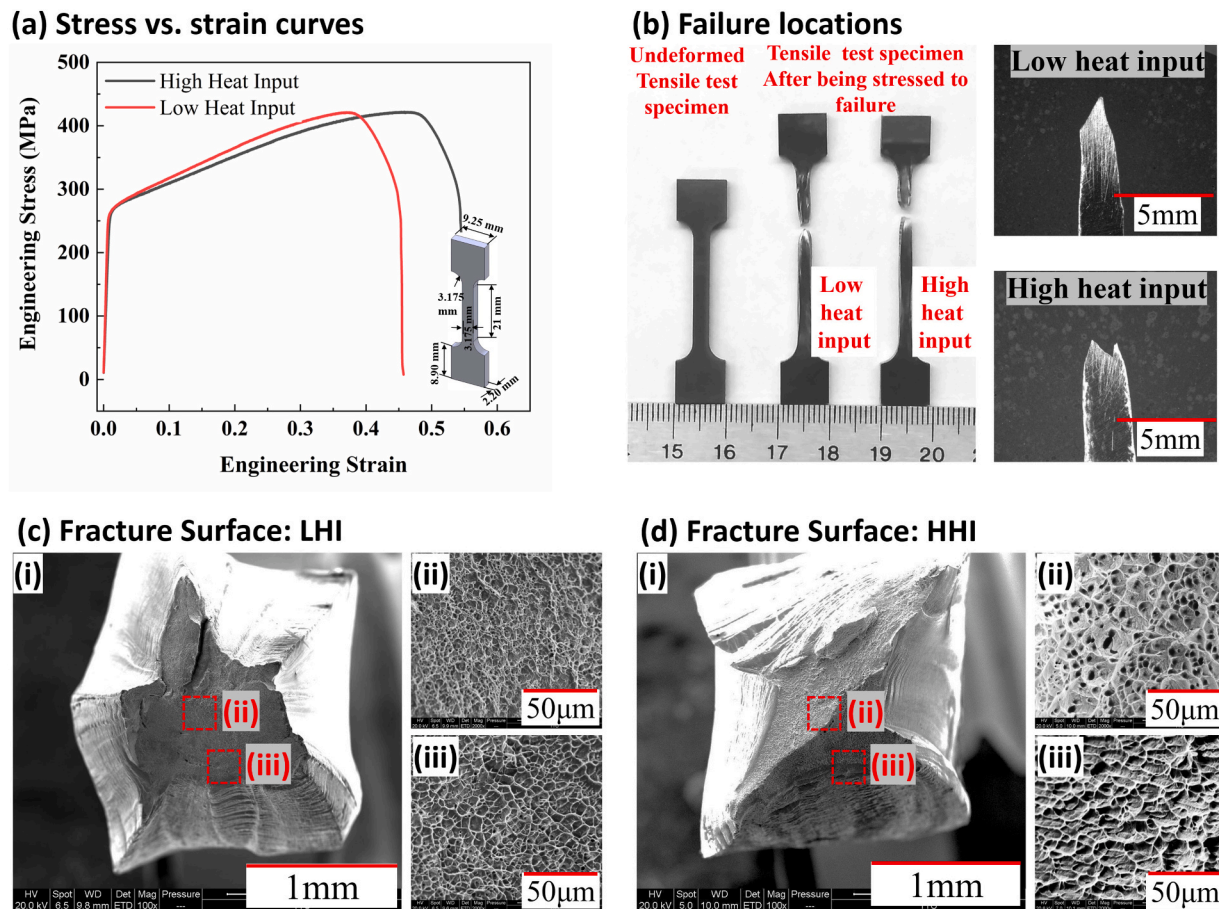
(a) Stress vs. strain curves

(b) Failure locations

(c) Fracture Surface: LHI

(d) Fracture Surface: HHI

Fig. 12. (a) Stress vs. strain curves for the tensile testing of the deposits with two heat input conditions; (b) OM images showing the failure locations; and SEM images of the fracture surfaces of the (c) low heat input and (d) high heat input specimens.

used.

4.2. Microstructures

The microstructure data presented in Figs. 9 and 10 show large elongated columnar grains with cellular dendritic substructures in both deposits. These columnar grains are formed due to the temperature gradient and the directional nature of cooling in WAAM [59,67]. The columnar grains in the HHI sample are significantly larger than the LHI one.

Although both deposits exhibit dendritic substructures at higher magnification in Fig. 10, these are observed to be significantly larger and elongated in the grain growth direction at HHI. In contrast, the dendritic substructures are almost equiaxed in the LHI condition. Similar observations on cellular- and columnar-dendritic substructures have been reported within the same deposit in WAAM of other materials [35]. The author reported smaller equiaxed substructures near the surface as a result of faster cooling, whereas elongated columnar morphology is observed at the center due to slower cooling [35]. As the LHI deposit cools down faster, the cellular substructures appear to be equiaxed. The higher thermal gradient coupled with a longer time required to cool down results in the formation of elongated cellular substructures in the HHI condition.

The HHI deposit is observed to have a larger grain size in this work (Fig. 9). A similar observation is also reported in CCW-AAM [34], showing increasing grain size with heat input. However, the CCW-AAM microstructure consisted of BCC + FCC phases with 67% ordered BCC (B2) phase [33,34] unlike the single-phase microstructure in the present work. This dual-phase microstructure in CCW-AAM is attributed to the

high Al content (20.18 at.%) in the deposit resulting from the wire-design strategy [33]. Although, the CCW-AAM deposit exhibited an almost identical composition of the major elements (Al, Co, Cr, Fe, and Ni) to the calculated one, the effect of other alloying elements (C, Mn, Si, P, S, and N) from the 304 stainless steel wire on the microstructure is unclear. Additionally, given the constraints of dimension and number of the constituting wires in combined cable wire, attaining a minuscule compositional adjustment might be difficult in the CCW-AAM approach. In contrast, the feedstock for GTA-WAAM is pre-alloyed with desired elements and can offer greater control over the composition and microstructure.
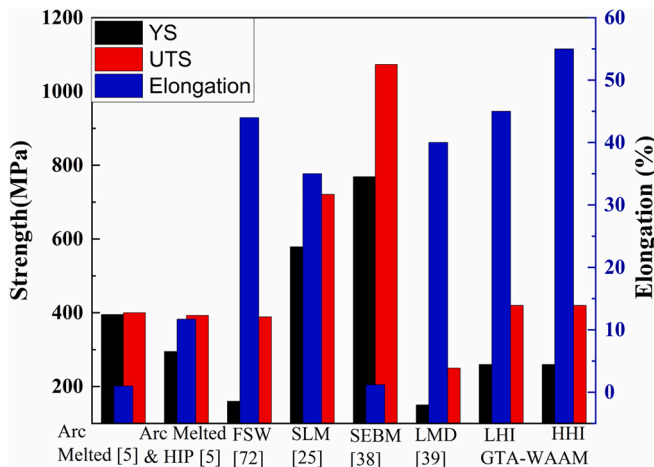
4.3. Mechanical properties

Mechanical properties of crystalline materials are strongly related to the dislocation motion in the solids [64]. Grain boundaries act as a barrier to dislocation propagation [68,69]. As the HEA deposits are mechanically tested only in the build direction in the present work, the grain boundaries are almost parallel to the applied stress. Hence, the dislocation motion is not significantly deterred by the grain boundaries. As a result, low yield strength and extremely high ductility are observed in both deposition conditions.

The mechanical testing results found in the present work are compared against the test results from other research on $Al_xCoCrFeNi$, including arc melting, welding, and AM processes. The results are summarized and graphically presented in Table 6 and Fig. 13, respectively. GTA-WAAM $Al_{0.1}CoCrFeNi$ has slightly low YS, comparable UTS, and significantly higher elongation, compared to arc-melted and arc-melted followed by HIPed specimens [5]. Unlike GTA-WAAM

Table 6
Mechanical properties of $Al_xCoCrFeNi$ HEA fabricated using different processes.

Fabrication process	Arc melted [5]	Arc melted and HIP [5]	Friction stir welded [70]	PBF		DED		
				SLM [25]	SEBM [26]	LMD [71]	GTA-WAAM	
							LHI	HHI
YS (MPa)	395	295	160	579	769	150	260	260
UTS (MPa)	400	393	389	721	1073	250	420	420
Elongation (%)	1	11.7	44	35	1.2	40	45	55

Fig. 13. Graphical representation of the mechanical properties of $Al_xCoCrFeNi$ HEA fabricated using different processes.

specimens, those processes exhibit much smaller equiaxed grains. Like other materials, finer grains are associated with higher YS and lower elongation in HEAs [70]. The large columnar grains, coupled with the orientation of tensile testing results in the slightly lower YS and high elongation in GTA-WAAM. Friction stir welding of $Al_{0.1}CoCrFeNi$ HEA results in a range of YS (160–544 MPa), UTS (389–730 MPa), and elongation (44–27.5%) [70], depending on the location. The coarse grain region is associated with low strength and high ductility. As the weld joints fail at the weakest point, only the data for the coarse grain area are considered for comparison. Among the various AM processes, the YS, UTS, and elongation are observed to vary widely. Among the PBF processes, Kuwabara et al. [26] reported a very high YS and UTS in a two-phase $Al_xCoCrFeNi$ HEA. But the elongation was significantly lower, compared to GTA-WAAM and other AM processes. Powder-fed DED using the LMD process on the other hand has a ductility comparable to the LHI condition of the GTA-WAAM. However, a significant amount of porosity is observed in the deposit, causing the strength to be significantly lower [71]. The work of Zhou et al. [25] reported a better strength and comparable ductility in SLM with $Al_{0.5}CoCrFeNi$ HEA. The high Al concentration in the composition of the HEA leads to the formation of the BCC phase, which has higher strength [72]. In their work on CCW-AAM of AlCoCrFeNi HEA, Shen et al. [34] also reported higher strength (975.53 MPa) at the cost of poor ductility (3.11) in as-deposited specimens as the microstructure was predominantly BCC and required subsequent heat-treatment to improve the ductility. However, a direct comparison of mechanical performance between GTA-WAAM and CCW-AAM cannot be drawn due to the vast difference in composition and resulting microstructure.

Based on the discussions, it can be concluded that the GTA-WAAM with pre-alloyed HEA wire offers comparable to superior strength, compared to traditional manufacturing processes like welding, and comparable mechanical properties to casting with good ductility, making it a suitable AM route for HEAs. Additionally, the pre-alloyed consumable wire offers greater control and accuracy over the composition and microstructure of the deposit.

The two different heat-input conditions have resulted in comparable microstructures and mechanical properties, with the HHI deposit having a better ductility. However, the HHI condition required less than half the number of layers (44 vs 89) to reach the same build height, making this a faster deposition condition. The surface quality and material efficiency are found to be significantly higher at the HHI. Based on these findings, the near-optimal process parameters can be considered the 200 A (Current), 2000 mm/min (WFS), and 200 mm/min (TS) in this study. However, a similar energy density and heat input can be attained with several different combinations, which may also produce quality deposits.

5. Conclusions

The statistical analysis, microstructure characterization, and mechanical testing results reveal that the GTA-WAAM with pre-alloyed wire can be a suitable alternative manufacturing route for the $Al_{0.1}CoCrFeNi$ HEA with predetermined composition. The results can be summarized as follows:

- The energy density is identified as the primary factor governing the bead continuity, and an energy density higher than 80 J/ mm^3 is required to deposit a uniform bead.
- For adequate energy density, a range of heat input conditions can be suitable with different travel speeds. Compared to the low heat input, the high heat input results in a faster build speed as well as improved material efficiency and surface quality. However, an extremely high heat input leads to a wide bead with a low profile, which will require more layers to be deposited to reach a certain height. Also, molten metal may drip once a certain deposit height is reached.
- Low and high heat input deposits have almost identical yield strength (260 MPa), ultimate tensile strength (420 MPa), and high ductility (45–55%), which are comparable to casting. The high heat input deposit has a better ductility (about 10% higher) and slightly lower hardness than the low heat input one.
- The low heat input deposit has a slightly higher hardness due to a higher dislocation density.
- The combination of 200A (Current), 2000 mm/min (wire feed speed), and 200 mm/min (travel speed) is identified as the near-optimal process parameters for GTA-WAAM of $Al_{0.1}CoCrFeNi$ high-entropy alloy.

Different combinations of process parameters (1) can also yield the same energy density and heat input and (2) can be used to produce high-quality material with varying microstructures and properties. The mechanical property evaluation in this study is performed only along the build direction. However, the test results may vary for different orientations. The authors will expand the work to provide a more extensive characterization of the microstructures, deformation mechanisms, and anisotropic mechanical properties.

Declaration of competing interest

The authors declare that they have no known competing financial

References

[1] Yeh JW, Chen SK, Lin SJ, Gan JY, Chin TS, Shun TT, et al. Nanostructured high-entropy alloys with multiple principal elements: novel alloy design concepts and outcomes. Adv Eng Mater 2004;6:299–303. https://doi.org/10.1002/adem.200300567.

[2] Yang Y, Zhao YL, Tong Y, Jiao ZB, Wei J, Cai JX, et al. Multicomponent intermetallic nanoparticles and superb mechanical behaviors of complex alloys. Science 2018;(362):933–7. https://doi.org/10.1126/science.aas8815 (80-).

[3] Gludovatz B, Hohenwarter A, Catoor D, Chang EH, George EP, Ritchie RO. A fracture-resistant high-entropy alloy for cryogenic applications. Science 2014; 345:1153–8. https://doi.org/10.1017/CBO9781107415324.004 (80-).

[4] Cantor B, Chang ITH, Knight P, Vincent AJB. Microstructural development in equiatomic multicomponent alloys. Mater Sci Eng A 2004;375–377:213–8. https://doi.org/10.1016/j.msea.2003.10.257.

[5] Tang Z, Santodonato LJ, Wang G, Liaw PK, Senkov ON, Parish CM, et al. Tensile ductility of an AlCoCrFeNi multi-phase high-entropy alloy through hot isostatic pressing (HIP) and homogenization. Mater Sci Eng A 2015;647:229–40. https://doi.org/10.1016/j.msea.2015.08.078.

[6] Huang H, Wu Y, He J, Wang H, Liu X, An K, et al. Phase-transformation ductilization of brittle high-entropy alloys via metastability engineering. Adv Mater 2017;29:1–7. https://doi.org/10.1002/adma.201701678.

[7] Lei Z, Liu X, Wu Y, Wang H, Jiang S, Wang S, et al. Enhanced strength and ductility in a high-entropy alloy via ordered oxygen complexes. Nature 2018;563:546–50. https://doi.org/10.1038/s41586-018-0685-y.

[8] Xia SQ, Wang Z, Yang TF, Zhang Y. Irradiation behavior in high entropy alloys. J Iron Steel Res Int 2015;22:879–84. https://doi.org/10.1016/S1006-706X(15)30084-4.

[9] Miracle DB. High entropy alloys as a bold step forward in alloy development. Nat Commun 2019;10:1–3. https://doi.org/10.1038/s41467-019-09700-1.

[10] Tsai MH, Yeh JW. High-entropy alloys: a critical review. Mater Res Lett 2014;2: 107–23. https://doi.org/10.1080/21663831.2014.912690.

[11] Ogura M, Fukushima T, Zeller R, Dederichs PH. Structure of the high-entropy alloy AlxCrFeCoNi: Fcc versus bcc. J Alloys Compd 2017;715:454–9. https://doi.org/10.1016/j.jallcom.2017.04.318.

[12] Qiu Z, Yao C, Feng K, Li Z, Chu PK. Cryogenic deformation mechanism of CrMnFeCoNi high-entropy alloy fabricated by laser additive manufacturing process. Int J Light Mater Manuf 2018;1:33–9. https://doi.org/10.1016/j.ijlmm.2018.02.001.

[13] Zhang Y, Zuo TT, Tang Z, Gao MC, Dahmen KA, Liaw PK, et al. Microstructures and properties of high-entropy alloys. Prog Mater Sci 2014;61:1–93. https://doi.org/10.1016/j.pmatsci.2013.10.001.

[14] Li X. Additive manufacturing of advanced multi-component alloys: bulk metallic glasses and high entropy alloys. Adv Eng Mater 2018;20:1–18. https://doi.org/10.1002/adem.201700874.

[15] Zhu ZG, Nguyen QB, Ng FL, An XH, Liao XZ, Liaw PK, et al. Hierarchical microstructure and strengthening mechanisms of a CoCrFeNiMn high entropy alloy additively manufactured by selective laser melting. Scr Mater 2018;154:20–4. https://doi.org/10.1016/j.scriptamat.2018.05.015.

[16] Niu PD, Li RD, Yuan TC, Zhu SY, Chen C, Wang MB, et al. Microstructures and properties of an equimolar AlCoCrFeNi high entropy alloy printed by selective laser melting. Intermetallics 2019;104:24–32. https://doi.org/10.1016/j.intermet.2018.10.018.

[17] Chen S, Tong Y, Liaw PK. Additive manufacturing of high-entropy alloys: a review. Entropy 2018:20. https://doi.org/10.3390/e20120937.

[18] Zhou R, Liu Y, Zhou C, Li S, Wu W, Song M, et al. Microstructures and mechanical properties of C-containing FeCoCrNi high-entropy alloy fabricated by selective laser melting. Intermetallics 2018;94:165–71. https://doi.org/10.1016/j.intermet.2018.01.002.

[19] Yim D, Kim HS. Fabrication of the high-entropy alloys and recent research trends: a review. J Korean Inst Met Mater 2017;55:671–83. https://doi.org/10.3365/KJMM.2017.55.10.671.

[20] Sun Z, Tan XP, Descoins M, Mangelinck D, Tor SB, Lim CS. Revealing hot tearing mechanism for an additively manufactured high-entropy alloy via selective laser melting. Scr Mater 2019;168:129–33. https://doi.org/10.1016/j.scriptamat.2019.04.036.

[21] Wang P, Huang P, Ng FL, Sin WJ, Lu S, Nai MLS, et al. Additively manufactured CoCrFeNiMn high-entropy alloy via pre-alloyed powder. Mater Des 2019;168: 107576. https://doi.org/10.1016/j.matdes.2018.107576.

[22] Ewald S, Kies F, Hermsen S, Voshage M, Haase C, Schleifenbaum JH. Rapid alloy development of extremely high-alloyed metals using powder blends in laser powder bed fusion. Materials (Basel) 2019;12:1–15. https://doi.org/10.3390/MA12101706.

[23] Kies F, Ikeda Y, Ewald S, Schleifenbaum JH, Hallstedt B, Körmann F, et al. Combined Al and C alloying enables mechanism-oriented design of multi-principal element alloys: Ab initio calculations and experiments. Scr Mater 2020;178: 366–71. https://doi.org/10.1016/j.scriptamat.2019.12.004.

[24] Karlsson D, Sahlberg M, Schneider JM, Jansson U, Marshal A, Johansson F, et al. Elemental segregation in an AlCoCrFeNi high-entropy alloy – a comparison between selective laser melting and induction melting. J Alloys Compd 2019;784: 195–203. https://doi.org/10.1016/j.jallcom.2018.12.267.

[25] Zhou PF, Xiao DH, Wu Z, Ou XQ. Al 0.5 FeCoCrNi high entropy alloy prepared by selective laser melting with gas-atomized pre-alloy powders. Mater Sci Eng A 2019; 739:86–9. https://doi.org/10.1016/j.msea.2018.10.035.

[26] Kuwabara K, Shiratori H, Fujieda T, Yamanaka K, Koizumi Y, Chiba A, et al. Mechanical and corrosion properties of AlCoCrFeNi high-entropy alloy fabricated with selective electron beam melting. Addit Manuf 2018;23:264–71. https://doi.org/10.1016/j.addma.2018.06.006.

[27] Dobbelstein H, Gurevich EL, George EP, Ostendorf A, Laplanche G. Laser metal deposition of a refractory TiZrNbHfTa high-entropy alloy. Addit Manuf 2018;24: 386–90. https://doi.org/10.1016/j.addma.2018.10.008.

[28] Xiang S, Li J, Luan H, Amarb A, Lud S, Lic K, et al. Effects of process parameters on microstructures and tensile properties of laser melting deposited CrMnFeCoNi high entropy alloys. Mater Sci Eng A 2019;743:412–7. https://doi.org/10.1016/j.msea.2019.03.010.

[29] Haase C, Tang F, Wilms MB, Weisheit A, Hallstedt B. Combining thermodynamic modeling and 3D printing of elemental powder blends for high-throughput investigation of high-entropy alloys – towards rapid alloy screening and design. Mater Sci Eng A 2017;688:180–9. https://doi.org/10.1016/j.msea.2017.01.099.

[30] Gao X, Lu Y. Laser 3D printing of CoCrFeMnNi high-entropy alloy. Mater Lett 2019; 236:77–80. https://doi.org/10.1016/j.matlet.2018.10.084.

[31] Williams SW, Martina F, Addison AC, Ding J, Pardal G, Colegrove P. Wire + arc additive manufacturing. Mater Sci Technol 2016;32:641–7. https://doi.org/10.1179/1743284715Y.0000000073.

[32] Gu J, Cong B, Ding J, Williams SW, Zhai Y. Wire+arc additive manufacturing of aluminium. SFF Symp Austin Texas; 2014. p. 451–8.

[33] Shen Q, Kong X, Chen X. Significant transitions of microstructure and mechanical properties in additively manufactured Al–Co–Cr–Fe–Ni high-entropy alloy under heat treatment. Mater Sci Eng A 2021;815. https://doi.org/10.1016/j.msea.2021.141257.

[34] Shen Q, Kong X, Chen X. Fabrication of bulk Al-Co-Cr-Fe-Ni high-entropy alloy using combined cable wire arc additive manufacturing (CCW-AAM): microstructure and mechanical properties. J Mater Sci Technol 2021;74:136–42. https://doi.org/10.1016/j.jmst.2020.10.037.

[35] Ahsan MRU, Tanvir ANM, Ross T, Elsawy A, Oh MS, Kim DB. Fabrication of bimetallic additively manufactured structure (BAMS) of low carbon steel and 316L austenitic stainless steel with wire + arc additive manufacturing. Rapid Prototyp J 2019. https://doi.org/10.1108/RPJ-09-2018-0235.

[36] Ahsan MRU, Kim YR, Ashiri R, Cho YJ, Eong CJ, Park YD. Cold metal transfer (CMT) GMAW of zinc-coated steel. Weld J 2016:95.

[37] Li Z, Zhao S, Diao H, Liaw PK, Meyers MA. High-velocity deformation of Al0.3 CoCrFeNi high-entropy alloy: remarkable resistance to shear failure. Sci Rep 2017; 7:1–8. https://doi.org/10.1038/srep42742.

[38] Niu S, Kou H, Guo T, Zhang Y, Wang J, Li J. Strengthening of nanoprecipitations in an annealed Al0.5CoCrFeNi high entropy alloy. Mater Sci Eng A 2016;671:82–6. https://doi.org/10.1016/j.msea.2016.06.040.

[39] Kumar N, Fusco M, Komarasamy M, Mishra RS, Bourham M, Murty KL. Understanding effect of 3.5 wt% NaCl on the corrosion of Al01CoCrFeNi high-entropy alloy495; 2017. p. 154–63. https://doi.org/10.1016/j.jnucmat.2017.08.015.

[40] Bramfitt BL, Benscoter AO. Metallographer's guide practices and procedures for irons and steelsvol. 95. ASM International; 2002.

[41] Rueden CT, Schindelin J, Hiner MC, DeZonia BE, Walter AE, Arena ET, et al. ImageJ2: ImageJ for the next generation of scientific image data. BMC Bioinformatics 2017;18:1–26. https://doi.org/10.1186/s12859-017-1934-z.

[42] Beausir B, Fundenberger J-J. Analysis tools for electron and X-ray diffraction, ATEX - software, www.atex-software.eu, Université de Lorraine - Metz. 2017 (http://www.atex-software.eu/help.html).

[43] ASTM E8. ASTM E8/E8M standard test methods for tension testing of metallic materials 1. Annu B ASTM Stand 2010;4:1–27. https://doi.org/10.1520/E0008.

[44] Dinovitzer M, Chen X, Laliberte J, Huang X, Frei H. Effect of wire and arc additive manufacturing (WAAM) process parameters on bead geometry and microstructure. Addit Manuf 2019;26:138–46. https://doi.org/10.1016/j.addma.2018.12.013.

[45] Messler RW. Principles of welding. WILEY-VCH Verlag GmbH & Co.; 2004.

[46] Gonçalves e Silva RH, Correa Riffel K, Pompermaier Okuyama M, Dalpiaz G. Effect of dynamic wire in the GTAW process. J Mater Process Technol 2019;269:91–101. https://doi.org/10.1016/j.jmatprotec.2019.01.033.

[47] Zhang Z, Chen X, Chen H, Zhong J, Chen S. Online welding quality monitoring based on feature extraction of arc voltage signal. Int J Adv Manuf Technol 2014;70: 1661–71. https://doi.org/10.1007/s00170-013-5402-2.

[48] Ahsan MRU, Cheepu M, Ashiri R, Kim TH, Jeong C, Park Y Do. Mechanisms of weld pool flow and slag formation location in cold metal transfer (CMT) gas metal arc welding (GMAW). Weld World 2017;61:1275–85. https://doi.org/10.1007/s40194-017-0489-y.

[49] Ahsan MRU, Kim YR, Kim CH, Kim JW, Ashiri R, Park YD. Porosity formation mechanisms in cold metal transfer (CMT) gas metal arc welding (GMAW) of zinc coated steels 2015;00:1–7. https://doi.org/10.1179/1362171815Y.0000000084.

[50] Tanvir ANM, Ahsan MRU, Ji C, Hawkins W, Bates B, Kim DB. Heat treatment effects on Inconel 625 components fabricated by wire + arc additive manufacturing (WAAM)—part 1: microstructural characterization. Int J Adv Manuf Technol 2019. https://doi.org/10.1007/s00170-019-03828-6.

[51] Ahsan MRU, Tanvir ANM, Seo GJ, Bates B, Hawkins W, Lee C, et al. Heat-treatment effects on a bimetallic additively-manufactured structure (BAMS) of the low-carbon steel and austenitic-stainless steel. Addit Manuf 2020;32:101036. https://doi.org/10.1016/j.addma.2020.101036.

[52] ISO/TC 213. Dimensional and geometrical product specifications and verification. ISO - ISO 4287:1997 - Geometrical Product Specifications (GPS) — surface texture: profile method — terms, definitions and surface texture parameters. 1997.

[53] Geng H, Li J, Xiong J, Lin X. Optimisation of interpass temperature and heat input for wire and arc additive manufacturing 5A06 aluminium alloy. Sci Technol Weld Join 2017;22:472–83. https://doi.org/10.1080/13621718.2016.1259031.

[54] Zhang Z, Sun C, Xu X, Liu L. Surface quality and forming characteristics of thin-wall aluminium alloy parts manufactured by laser assisted MIG arc additive manufacturing. Int J Light Mater Manuf 2018;1:89–95. https://doi.org/10.1016/j.ijlmm.2018.03.005.

[55] Sokkalingam R, Muthupandi V, Sivaprasad K, Prashanth G. Dissimilar welding of Al0.1CoCrFeNi high-entropy alloy and AISI304 stainless steel. J Mater Res 2019; 34:2683–94. https://doi.org/10.1557/jmr.2019.186.

[56] Wang W, Wang W, Wang S, Tsai Y, Lai C, Yeh J. Effects of Al addition on the microstructure and mechanical property of Al$_x$CoCrFeNi high-entropy alloys. Intermetallics 2012;26:44–51. https://doi.org/10.1016/j.intermet.2012.03.005.

[57] Hall EO. Variation of hardness of metals with grain size [5]. Nature 1954;173: 948–9. https://doi.org/10.1038/173948b0.

[58] Lim YY, Chaudhri MM. The influence of grain size on the indentation hardness of high-purity copper and aluminium. Philos Mag A Phys Condens Matter, Struct Defects Mech Prop 2002;82:2071–80. https://doi.org/10.1080/01418610208235717.

[59] Wu Q, Ma Z, Chen G, Liu C, Ma D, Ma S. Obtaining fine microstructure and unsupported overhangs by low heat input pulse arc additive manufacturing. J Manuf Process 2017;27:198–206. https://doi.org/10.1016/j.jmapro.2017.05.004.

[60] Yang T, Tang Z, Xie X, Carroll R, Wang G, Wang Y, et al. Deformation mechanisms of Al 0. 1 CoCrFeNi at elevated temperaturesvol. 684; 2017. p. 552–8. https://doi.org/10.1016/j.msea.2016.12.110.

[61] Wu SW, Wang G, Yi J, Jia YD, Hussain I, Zhai QJ, et al. Strong grain-size effect on deformation twinning of an Al0.1CoCrFeNi high-entropy alloy. 2017. p. 3831. https://doi.org/10.1080/21663831.2016.1257514.

[62] Luo S, Gao P, Yu H, Yang J, Wang Z, Zeng X. Selective laser melting of an equiatomic AlCrCuFeNi high-entropy alloy: processability, non-equilibrium microstructure and mechanical behavior. J Alloys Compd 2019;771:387–97. https://doi.org/10.1016/j.jallcom.2018.08.290.

[63] Zhang M, Zhou X, Wang D, Zhu W, Li J, Zhao YF. AlCoCuFeNi high-entropy alloy with tailored microstructure and outstanding compressive properties fabricated via selective laser melting with heat treatment. Mater Sci Eng A 2019;743:773–84. https://doi.org/10.1016/j.msea.2018.11.118.

[64] Hertzberg RW, Vinci RP, Hertzberg JL. Deformation and fracture mechanics of engineering materials. 5th ed. John Wiley & Sons, Inc.; 2012. https://doi.org/10.1016/b978-0-08-026167-6.50013-8.

[65] Benakis M, Costanzo D, Patran A. Current mode effects on weld bead geometry and heat affected zone in pulsed wire arc additive manufacturing of Ti-6-4 and Inconel 718. J Manuf Process 2020;60:61–74. https://doi.org/10.1016/j.jmapro.2020.10.018.

[66] Yildiz AS, Davut K, Koc B, Yilmaz O. Wire arc additive manufacturing of high-strength low alloy steels: study of process parameters and their influence on the bead geometry and mechanical characteristics. Int J Adv Manuf Technol 2020;108: 3391–404. https://doi.org/10.1007/s00170-020-05482-9.

[67] Li Z, Liu C, Xu T, Ji L, Wang D, Lu J, et al. Reducing arc heat input and obtaining equiaxed grains by hot-wire method during arc additive manufacturing titanium alloy. Mater Sci Eng A 2019;742:287–94. https://doi.org/10.1016/j.msea.2018.11.022.

[68] Yoo YSJ, Book TA, Sangid MD, Kacher J. Identifying strain localization and dislocation processes in fatigued Inconel 718 manufactured from selective laser melting. Mater Sci Eng A 2018;724:444–51. https://doi.org/10.1016/j.msea.2018.03.127.

[69] Lee WS, Liu CY, Sun TN. Deformation behavior of Inconel 690 super alloy evaluated by impact test. J Mater Process Technol 2004;153–154:219–25. https://doi.org/10.1016/j.jmatprotec.2004.04.275.

[70] Komarasamy M, Kumar N, Tang Z, Mishra RS, Liaw PK. Effect of microstructure on the deformation mechanism of friction stir-processed Al0.1CoCrFeNi high entropy alloy. Mater Res Lett 2014;3:30–4. https://doi.org/10.1080/21663831.2014.958586.

[71] Joseph J, Hodgson P, Jarvis T, Wu X, Stanford N, Fabijanic DM. Effect of hot isostatic pressing on the microstructure and mechanical properties of additive manufactured Al$_x$CoCrFeNi high entropy alloys. Mater Sci Eng A 2018;717:11–9. https://doi.org/10.1016/j.msea.2018.01.063.

[72] Jiao Q, Sim GD, Komarasamy M, Mishra RS, Liaw PK, El-Awady JA. Thermo-mechanical response of single-phase face-centered-cubic Al$_x$CoCrFeNi high-entropy alloy microcrystals. Mater Res Lett 2018;6:300–6. https://doi.org/10.1080/21663831.2018.1446468.